



CrossMark

Gas-phase Synthesis of Silaformaldehyde (H_2SiO) and Hydroxysilylene (HSiOH) in Outflows of Oxygen-rich Asymptotic Giant Branch Stars

Chao He¹, Srinivas Doddipatla¹, Zhenghai Yang¹, Shane J. Goettl¹ , Ralf I. Kaiser¹ , Valeriy N. Azyazov², Alexander M. Mebel³ , and Tom J. Millar⁴ 

¹ Department of Chemistry, University of Hawai'i at Manoa, Honolulu, HI 96822, USA; ralfk@hawaii.edu

² Lebedev Physical Institute, Samara 443011, Russian Federation

³ Department of Chemistry and Biochemistry, Florida International University, Miami, FL 33199, USA; mebela@fiu.edu

⁴ School of Mathematics and Physics, Queen's University Belfast, University Road, Belfast BT7 1NN, UK; Tom.Millar@qub.ac.uk

Received 2021 May 16; revised 2021 September 27; accepted 2021 September 30; published 2021 October 27

Abstract

Silicon- and oxygen-containing species such as silicon monoxide (SiO) and silicon dioxide (SiO_2) represent basic molecular building blocks connected to the growth of silicate grains in outflows of oxygen-rich asymptotic giant branch (AGB) stars like R Doradus. Yet the fundamental mechanisms of the formation of silicate grains and the early processes that initiate the coupling of the silicon with the oxygen chemistries in circumstellar envelopes have remained obscure. Here, in a crossed molecular beams experiment combined with ab initio electronic structure calculations, we reveal that at least the *d*2-silaformaldehyde (D_2SiO) and *d*2-hydroxysilylene (DSiOD) molecules—proxies for the astronomically elusive silaformaldehyde (H_2SiO) and hydroxysilylene (HSiOH) molecules—can be synthesized via the reaction of the D1-silyldiyne radical (SiD ; $\text{X}^2\Pi$) with D2-water (D_2O) under single-collision conditions. This system represents a benchmark of a previously overlooked class of reactions, in which the silicon–oxygen bond coupling can be initiated by a reaction between the simplest silicon-bearing radical (silyldiyne) and one of the most abundant species in the circumstellar envelopes of evolved oxygen-rich AGB stars (water). As supported by novel astrochemical modeling, considering that silicon- and oxygen-containing species like H_2SiO and HSiOH might be photolyzed easily, they ultimately connect to simple molecular precursors such as SiO that drive a chain of reactions conceivably forming higher molecular weight silicon oxides and, ultimately, a population of silicates at high temperatures.

Unified Astronomy Thesaurus concepts: [Astrochemistry \(75\)](#); [Interstellar dust \(836\)](#); [Laboratory astrophysics \(2004\)](#); [Circumstellar envelopes \(237\)](#)

1. Introduction

In recent decades, silicon- and oxygen-containing molecules like silicon monoxide (SiO ; Reber et al. 2006, 2008; Gail et al. 2013; Liu & Jiang 2017; Takigawa et al. 2017; Cigan et al. 2019; Escatllar & Bromley 2020) and silicon dioxide (SiO_2 ; Fabian et al. 2000; Li & Draine 2002; Schneider et al. 2004; Nozawa et al. 2005; Loeffler et al. 2016) have been recognized as fundamental molecular building blocks eventually leading to the formation of silicate grains—nanoparticles consisting primarily of olivine-type ($(\text{Mg},\text{Fe})_2\text{SiO}_4$) refractory minerals—in outflows of oxygen-rich asymptotic giant branch (AGB) stars like R Doradus and potentially in cold molecular clouds such as the Taurus molecular cloud 1 (TMC-1; Avramov et al. 2005; Ziurys 2006; Henning 2010; Jones & Nuth 2011; Goumans & Bromley 2012; Tielens 2012; Krasnokutski et al. 2014). However, the elementary reactions initiating and driving the complex networks of chemical reactions and molecular mass growth processes are still very contentious. This is because interstellar silicates are destroyed faster by sputtering from galactic cosmic rays once ejected into the interstellar medium (ISM) than synthesized during the late stages of stellar evolution through nucleation and reactions of silicon-/oxygen-bearing molecules together with magnesium-type and iron-based oxides in circumstellar envelopes (CSEs) of oxygen-rich AGB and red supergiant stars (Gail & Sedlmayr 1999; Reber et al. 2006; Ziurys 2006; Reber et al. 2008; Henning 2010; Jones & Nuth 2011; Goumans & Bromley 2012; Tielens 2012; Gail et al. 2013; Gobrecht et al. 2016). This inconsistency is

reflected in the lifetimes of interstellar grains of a few 10^8 yr compared to their formation rates of 3×10^9 yr (Tielens 1998; Draine 2009; Jones & Nuth 2011; Dwek 2016). Therefore, critical elementary reactions that involved in the mass growth processes of silicate grains are lacking. Interstellar silicates play a crucial role in star formation and hence in the origin of solar systems by impacting the radiation balance and in their role as “molecular factories” through the synthesis of complex organic molecules within their ice-coated surfaces (Abplanalp et al. 2016). Since even amino acids and (precursors to) sugars can be formed throughout their ice-coated surfaces through interaction with ionizing radiation in the form of energetic galactic cosmic rays and the internal vacuum ultraviolet radiation field present even deep inside molecular clouds, these nanoparticles have also been linked to the prebiotic evolution of the ISM (Wakelam et al. 2010). Consequently, the unraveling of the origin of silicates is of critical significance to the astrochemistry, astrobiology, and astrophysics communities to ultimately untangle the most fundamental processes that drive the formation of solar systems, including our own.

Here we reveal that the silaformaldehyde molecule (H_2SiO) and hydroxysilylene (HSiOH)—the isovalent species of the ubiquitous interstellar formaldehyde molecule (H_2CO ; Fu et al. 2012), along with hydroxymethylene (HCOH ; Mazarei & Mousavipour 2017; Simmie & Würmel 2020; Figure 1)—can be proficiently prepared through a high-temperature gas-phase chemistry. In a combined crossed molecular beam and electronic structure study, we report the formation of hitherto astronomically elusive *d*2-silaformaldehyde (D_2SiO) and *d*2-

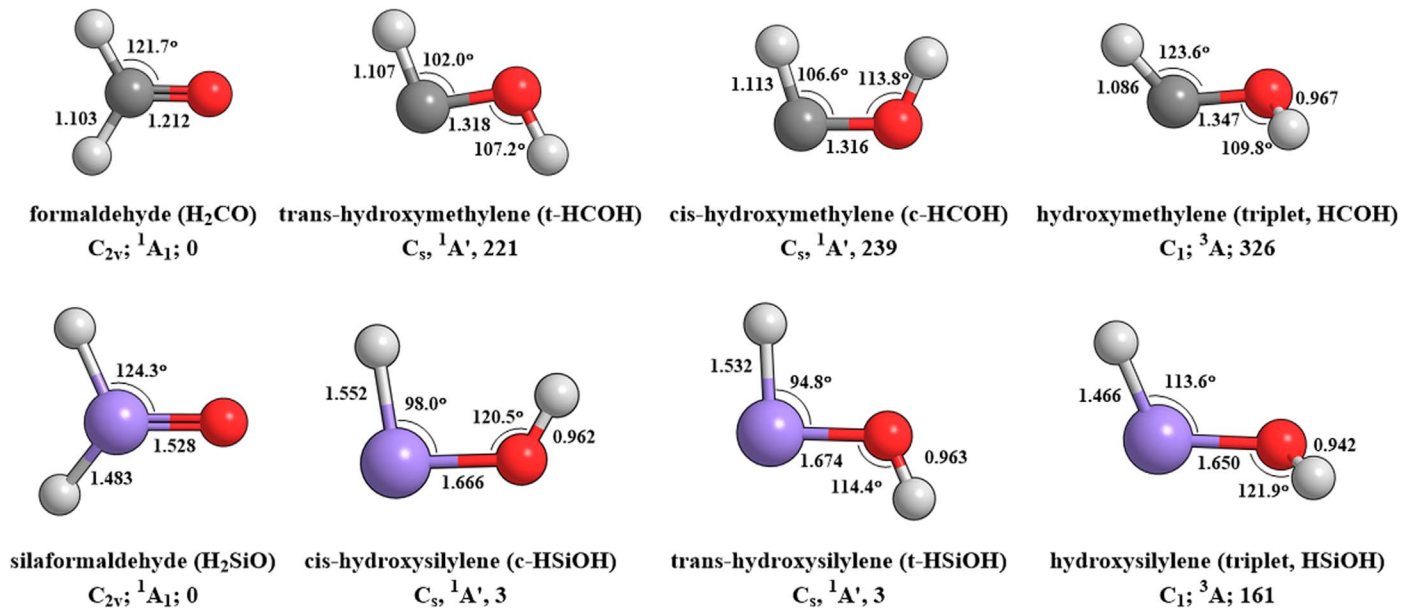


Figure 1. Molecular structures, point groups, relative energies (kJ mol⁻¹), bond distances (Å), and selected bond angles of formaldehyde (H₂CO), silaformaldehyde (H₂SiO), and their isomers. Carbon, silicon, oxygen, and hydrogen atoms are color coded in black, purple, red, and gray, respectively.

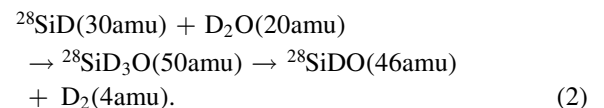
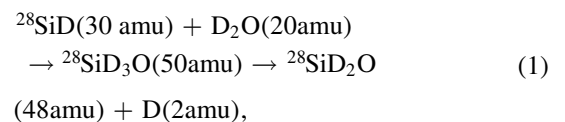
hydroxysilylene (DSiOD)—as a proxy for H₂SiO and HSiOH—via the bimolecular reaction of the D1-silyldyne radical (SiD; X²Π) with D₂-water (D₂O). This system exemplifies the surrogate for the reaction of the silyldyne radical (SiH) generated via photodissociation of silane (SiH₄; Glenewinkel-Meyer et al. 1993) with water (H₂O) to prepare gas-phase silaformaldehyde (H₂SiO) and hydroxysilylene (HSiOH) via a single collision event. This bimolecular reaction may represent a critical pathway to H₂SiO and HSiOH in high-temperature environments, such as the outflows of oxygen-rich AGB stars. Along with SiO and SiO₂, H₂SiO and HSiOH could drive a chain of reactions conceivably forming higher molecular weight silicon oxides and, ultimately, a population of silicates at high temperatures.

2. Results

2.1. Crossed Molecular Beam Studies: Laboratory and Center-of-mass Frame

The gas-phase reaction of the D1-silyldyne radical (SiD; X²Π) with D₂-water (D₂O; X¹A₁) was studied under single-collision conditions in a crossed molecular beam machine (Yang et al. 2021). Considering the natural isotope abundances of silicon (²⁸Si: 92.23%; ²⁹Si: 4.67%; ³⁰Si: 3.10%), the reactive scattering signal was collected at a mass-to-charge (m/z) of $m/z = 48$ and 46, which are related to the potential products upon the emission of atomic (²⁸SiD₂O⁺; $m/z = 48$; reaction (1)) and molecular deuterium (²⁸SiDO⁺; $m/z = 46$; ³⁰SiDO⁺; $m/z = 48$; reaction (2)) and fragments generated via dissociative electron impact ionization of the parent molecule leading to ²⁸SiDO⁺ ($m/z = 46$). Time-of-flight (TOF) spectra were accumulated for up to 96 hr at each angle with ion counts at $m/z = 46$ emerging at a level of 50% ± 3% compared to $m/z = 48$. These TOF spectra are superimposable after scaling (Figure A1); along with the isotopic substitution pattern, this finding suggests the existence of a single reaction channel, i.e., the reaction of the D1-silyldyne radical (SiD; X²Π) with D₂O forming SiD₂O isomer(s)—predominantly via the reaction of ²⁸SiD—along with the emission of atomic deuterium (D; 2 amu), yielding the

signal at $m/z = 48$ (²⁸SiD₂O, hereafter SiD₂O). The signal at $m/z = 46$ originates from dissociative electron impact ionization of the parent molecules. Consequently, the laboratory data suggest that the reaction of the D1-silyldyne radical (SiD; X²Π) with D₂O involves the formation of SiD₂O isomer(s) via the atomic deuterium emission. The resulting TOF spectra and the full laboratory angular distributions were collected at the best signal-to-noise ratio at $m/z = 48$ (SiD₂O⁺; Figure 2). This distribution is almost forward-backward symmetric around the center-of-mass (CM) angle of 43°:3 (Table A1) and spans a scattering angular range from 28°:3 to 58°:3. These results indicate that the reaction proceeds via indirect scattering dynamics involving the existence of SiD₃O intermediate(s) that ultimately dissociate to SiD₂O via atomic deuterium emission (Levine 2005). Note that, accounting for distinct recoil circles for the atomic and molecular deuterium loss channels (Figure A2), the ratio of the ion counts at $m/z = 48$ (reaction (1)) versus 46 (reaction (2)) is determined to be 1 ($m/z = 48$):0.04 ± 0.01 ($m/z = 46$). This may explain that the products of reaction (2) cannot be detected under our experimental conditions compared with the already weak scattering signal for reaction (1):



Our primary objective is to explore the nature of the SiD₂O isomer(s) along with the underlying reaction mechanism(s) on the pertinent SiD₃O potential energy surface(s) (PESs) accessed through the bimolecular reaction of the D1-silyldyne radical (SiD; X²Π) with D₂O. To reach these goals, a forward convolution of the laboratory data into the CM reference frame generates the CM translational energy $P(E_T)$ and angular $T(\theta)$ flux distributions

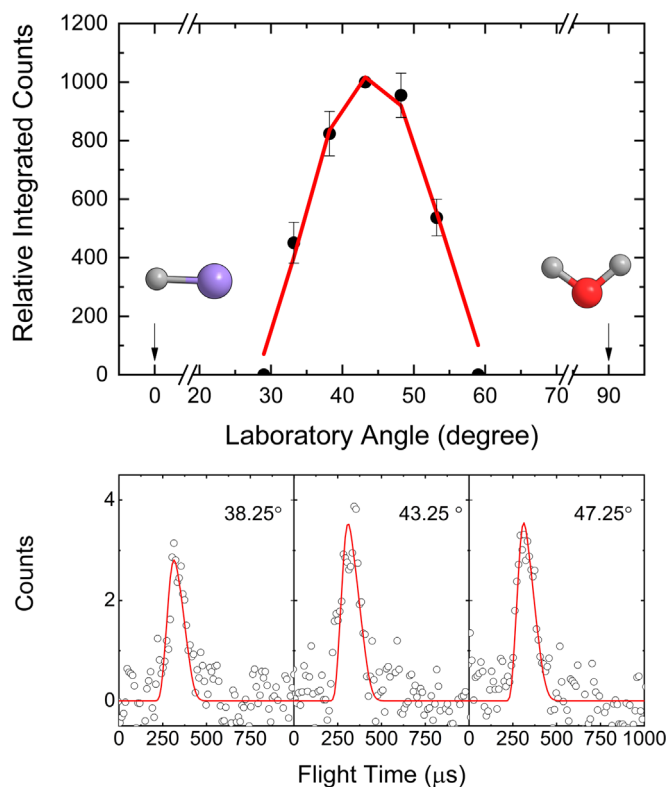


Figure 2. Laboratory angular distribution (top) and TOF spectra (bottom) collected at $m/z = 48$ for the reaction of the D1-silyldiyne radical (SiD; $X^2\Pi$) with D2-water (D_2O). The black circles represent the experimental data, while the red lines define the best fits.

(Figure 3; Yang et al. 2021) via a transformation of the laboratory data to the CM frame. Within our error limits, the resulting best-fit CM functions (Figure 3) were achieved using a single channel of the product mass combination of 48 amu (SiD_2O) plus 2 amu (D). The resulting CM translational energy distribution $P(E_T)$ reveals a maximum translational energy release (E_{max}) of 37 ± 10 kJ mol $^{-1}$. Considering the energy conservation, the maximum translational energy (E_{max}), collision energy (E_C), and reaction energy ($\Delta_r G$) are connected via $E_{max} = E_C - \Delta_r G$ with regard to the molecules born without rovibrational excitation. Therefore, the reaction energy is calculated to be -10 ± 10 kJ mol $^{-1}$. Furthermore, the $P(E_T)$ distribution peaked away from zero translational energy at 19 ± 5 kJ mol $^{-1}$, suggesting a tight exit transition state leading to SiD_2O molecules from the SiD_3O intermediates (Levine 2005). Further, the average translational energy of the products was derived to be 18 ± 5 kJ mol $^{-1}$, suggesting that $49\% \pm 13\%$ of the available energy is transformed into the translational degrees of freedom of the products. Finally, the resulting CM angular distribution $T(\theta)$ depicts nonzero intensity over the complete scattering range from 0° to 180° , proposing indirect scattering dynamics via the formation of SiD_3O complex(es); the forward-backward symmetry of $T(\theta)$ implies that the lifetime of the decomposing SiD_3O complex is longer than the rotational period (s) (Miller et al. 1967).

2.2. Electronic Structure Calculations and Reaction Mechanism

The electronic structure calculations identified the existence of two distinct SiDO isomers (**p1**–**p2**) that may be produced via molecular deuterium loss; further, four SiD_2O isomers (**p3**–**p6**)

were identified that can be accessed through atomic deuterium emission (Figure 4). Our computations suggest that the reaction is initiated by the barrierless formation of a complex **i1**, which is stabilized by 50 kJ mol $^{-1}$ with respect to the separated reactants and bound through a dative bond formed by donation of the lone oxygen atom to the empty p orbital of Si. This complex isomerizes via deuterium migration from the oxygen atom of the water to the SiD moiety, leading to the hydroxy-*d3*-silyl radical (D_2SiOD , **i2**, X^1A') with an inherent barrier of 32 ± 5 kJ mol $^{-1}$. The hydroxy-*d3*-silyl radical represents the global minimum of the SiD_3O PES. Our calculations also identified that a molecular deuterium loss from **i1** yields the product hydroxy-*d*-silyldiyne ($SiOD$, **p1**, X^1A' , $\Delta_r G = -131 \pm 5$ kJ mol $^{-1}$) with an inherent barrier of 27 ± 5 kJ mol $^{-1}$. Intermediate **i1** can emit atomic deuterium from the silicon atom, forming a van der Waals complex silicon-D2-water ($SiOD_2$, **p6**, $^3A''$, $\Delta_r G = 256 \pm 5$ kJ mol $^{-1}$) in an overall endoergic reaction. The products trans-*d2*-hydroxysilylene (t- $DSiOD$, **p4**, X^1A' , $\Delta_r G = -5 \pm 5$ kJ mol $^{-1}$) and cis-*d2*-hydroxysilylene (c- $DSiOD$, **p5**, X^1A' , $\Delta_r G = -5 \pm 5$ kJ mol $^{-1}$) can also be produced via atomic deuterium loss from **i1** with transition states located 79 and 86 kJ mol $^{-1}$ above the separated products, respectively. Note that the pathways **i1** \rightarrow **p4**/**p5** are not competitive due to the transition states ranging well above our collision energy of 27.3 ± 0.5 kJ mol $^{-1}$, which cannot be overcome under our experimental conditions. Intermediate **i2** can isomerize via a deuterium shift from the oxygen atom to the silicon atom, yielding the *d3*-silyloxy intermediate (D_3SiO , **i3**, $^1A'$) via a barrier of 188 kJ mol $^{-1}$ above intermediate **i2**. The product hydroxy-*d*-silyldiyne ($SiOD$, **p1**, X^1A') can be accessed via molecular deuterium loss from **i2** via a tight exit transition barrier lying 100 kJ mol $^{-1}$ above the separated products, while the products *d2*-silaformaldehyde (D_2SiO , **p3**, X^1A' , $\Delta_r G = -8 \pm 5$ kJ mol $^{-1}$), trans-*d2*-hydroxysilylene (t- $DSiOD$, **p4**, X^1A' , $\Delta_r G = -5 \pm 5$ kJ mol $^{-1}$), and cis-*d2*-hydroxysilylene (c- $DSiOD$, **p5**, X^1A' , $\Delta_r G = -5 \pm 5$ kJ mol $^{-1}$) can be formed via atomic deuterium loss from **i2**. Here the formation of *d2*-silaformaldehyde (D_2SiO , **p3**) occurs via an exit barrier of 18 kJ mol $^{-1}$, whereas **p4** and **p5** are produced via loose transition states without distinct exit barriers. The decomposition of **i3** yields the product oxo-silyl-*d* ($DSiO$, **p2**, $^1A'$, $\Delta_r G = -95 \pm 5$ kJ mol $^{-1}$) via a molecular deuterium loss from **i3** via a tight exit transition state lying 96 kJ mol $^{-1}$ above the separated products. The product *d2*-silaformaldehyde (D_2SiO ; **p3**) can be formed via atomic deuterium emission from **i3** via a loose transition state.

We are now merging our experimental findings with the results from the ab initio calculations to propose the underlying reaction mechanism(s) along with the chemical dynamics of the reaction. The experimentally derived reaction energy of -10 ± 10 kJ mol $^{-1}$ is in good agreement with our computed value for an exoergic reaction of -8 ± 5 and -5 ± 5 kJ mol $^{-1}$ to synthesize the *d2*-silaformaldehyde (D_2SiO , **p3**, $\Delta_r G = -8 \pm 5$ kJ mol $^{-1}$), trans-*d2*-hydroxysilylene (t- $DSiOD$, **p4**, $\Delta_r G = -5 \pm 5$ kJ mol $^{-1}$), and/or cis-*d2*-hydroxysilylene (c- $DSiOD$, **p5**, $\Delta_r G = -5 \pm 5$ kJ mol $^{-1}$) along with atomic deuterium. The silicon-D2-water complex ($SiOD_2$, **p6**, $\Delta_r G = 256 \pm 5$ kJ mol $^{-1}$) is energetically not available considering the collision energy (E_C) of 27.3 kJ mol $^{-1}$. Consequently, we deduce that the *d2*-silaformaldehyde (D_2SiO ; **p3**), trans-*d2*-hydroxysilylene (t- $DSiOD$; **p4**), and/or cis-*d2*-hydroxysilylene (c- $DSiOD$; **p5**) are formed in the crossed molecular beam reaction of the D1-silyldiyne radical (SiD; $X^2\Pi$) with D_2O . The reaction of the D1-silyldiyne radical (SiD; $X^2\Pi$) with D_2O proceeds via indirect scattering dynamics (complex

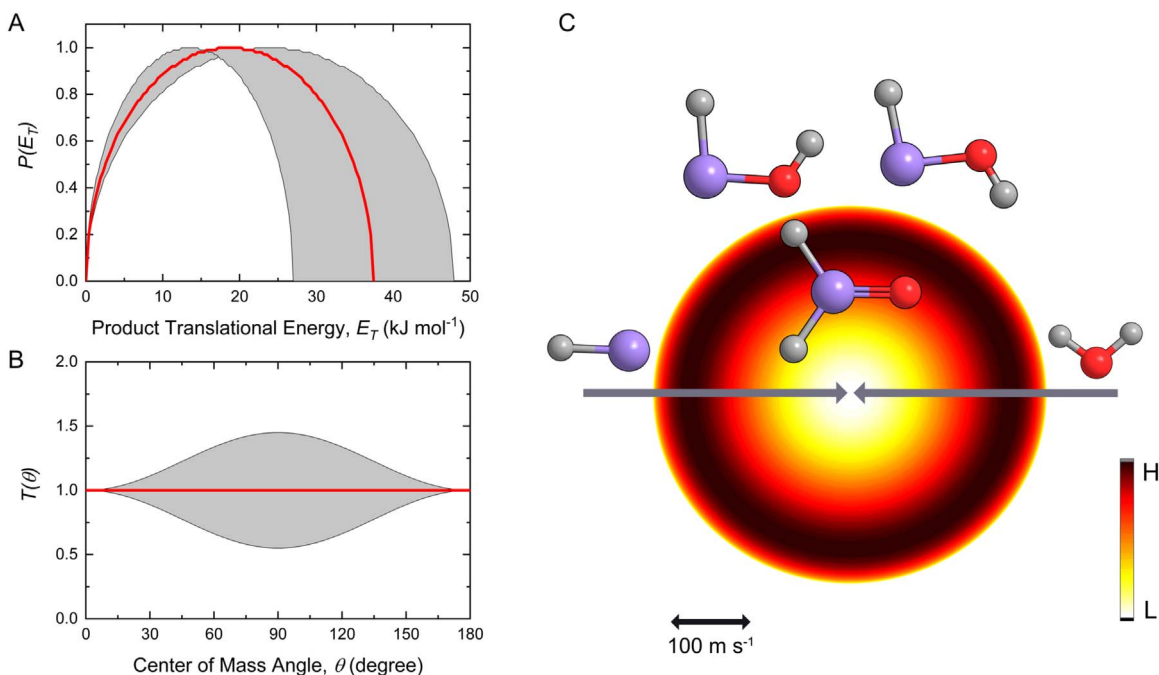


Figure 3. The CM translational energy flux distribution (a), the CM angular flux distribution (b), and the top view of the corresponding flux contour map (c) leading to the formation of *d2*-silaformaldehyde (D_2SiO) and *d2*-hydroxysilylene (cis-DSiOD and trans-DSiOD) plus atomic deuterium in the D1-silylydyne radical (SiD; $X^2\Pi$) with D_2 -water (D_2O) system. Shaded areas indicate the acceptable upper and lower error limits, while the red solid lines define the best fits. The flux contour map represents the flux intensity of the reactively scattered heavy products as a function of the CM scattering angle (θ) and product velocity (u). The color bar manifests the flux gradient from high (H) to low (L) intensity. The colors of the atoms are as follows: silicon (purple), oxygen (red), and deuterium (gray).

forming reaction) and is initiated with the formation of a bound dative complex **i1**. The collision complex **i1** undergoes atomic deuterium migration to **i2**, with the latter ejecting a deuterium atom to form the products *d2*-silaformaldehyde (D_2SiO , **p3**, X^1A' , $\Delta_rG = -8 \pm 5$ kJ mol⁻¹), trans-*d2*-hydroxysilylene (t-DSiOD, **p4**, X^1A' , $\Delta_rG = -5 \pm 5$ kJ mol⁻¹), and/or cis-*d2*-hydroxysilylene (c-DSiOD, **p5**, X^1A' , $\Delta_rG = -5 \pm 5$ kJ mol⁻¹). The product *d2*-silaformaldehyde (D_2SiO , **p3**, X^1A' , $\Delta_rG = -8 \pm 5$ kJ mol⁻¹) can also be formed via the atomic deuterium emission from intermediate **i3**, which stems from the deuterium shift from the OD group to SiD₂ moiety in **i2**. It is instructive to compare the present results of the electronic structure calculations on the SiH₃O PES with those reported by Zachariah & Tsang (1995), who explored the thermochemistry, energetics, and kinetics of high-temperature Si_xH_yO_z reactions at the BAC-MP4 level of theory including, in particular, unimolecular decomposition of H₂SiOH and H₃SiO and its reverse reactions, although the SiH + H₂O channel was not considered in either direction. The agreement appears to be rather close, as the average unsigned difference in the relative energies of various species and barrier heights is only 6 kJ mol⁻¹, and the maximal deviation is 14 kJ mol⁻¹.

To assess to what extent **p3–p5** could be formed in this experiment, we calculated the statistical yields of products **p1–p6** using Rice–Ramsperger–Kassel–Marcus (RRKM) theory (Table A3). These studies reveal that *d2*-silaformaldehyde (D_2SiO , **p3**), trans-*d2*-hydroxysilylene (t-DSiOD, **p4**), and cis-*d2*-hydroxysilylene (c-DSiOD, **p5**) contribute 25%, 26%, and 49%, respectively, at $E_C = 27.3$ kJ mol⁻¹. For the product *d2*-silaformaldehyde (D_2SiO , **p3**), dissociation from **i2** and **i3** supplies 2% and 23%, respectively. Since the isomerization of **i1** to **i2** is a key link to form the products *d2*-silaformaldehyde (D_2SiO , **p3**), trans-*d2*-hydroxysilylene (t-DSiOD, **p4**), and cis-*d2*-hydroxysilylene (c-DSiOD, **p5**) along with the atomic

deuterium, it is critical to recall that a fit of the experimental data had to be obtained via the combination of a reaction threshold of 27–32 kJ mol⁻¹ with the fitting routine. In the fitting program, the collision energy (E_C) and velocity distribution of each supersonic beam $f(v_i)$, with i being the primary SiD and secondary D_2O beam, are defined by

$$E_C = \frac{1}{2} \mu \nu_r^2, \quad (3)$$

$$\mu = \frac{m_{SiD} * m_{D_2O}}{m_{SiD} + m_{D_2O}}, \quad (4)$$

$$\nu_r^2 = \nu_{SiD}^2 + \nu_{D_2O}^2, \quad (5)$$

$$f(v_{SiD}) \propto v_{SiD}^2 \exp\left(-\left(\frac{v_{SiD}}{\alpha_{SiD}} - S_{SiD}\right)^2\right), \quad (6)$$

$$f(v_{D_2O}) \propto v_{D_2O}^2 \exp\left(-\left(\frac{v_{D_2O}}{\alpha_{D_2O}} - S_{D_2O}\right)^2\right), \quad (7)$$

with the relative velocity ν_r , velocity v_i , reduced mass μ , mass of the reactant m , velocity v_i , speed ratio S_i , $\alpha_i = (2kT/m_i)^{1/2}$, temperature of the beam T , and Boltzmann's constant k . The fitting program convolutes over the apparatus functions including the velocity distributions and the velocity spreads. The corresponding relative velocity peaked at 2133 m s⁻¹, yielding a peak collision energy of $E_C = 27.3 \pm 3.4$ kJ mol⁻¹. Considering the computed barrier of the reaction connecting **i1** and **i2** of 32 ± 5 kJ mol⁻¹, around 50% of the collisions are sufficiently high to overcome this isomerization barrier. The resulting reaction cross section (σ) increases as the collision energy increases (Equation (8)), with E_0 denoting the inherent

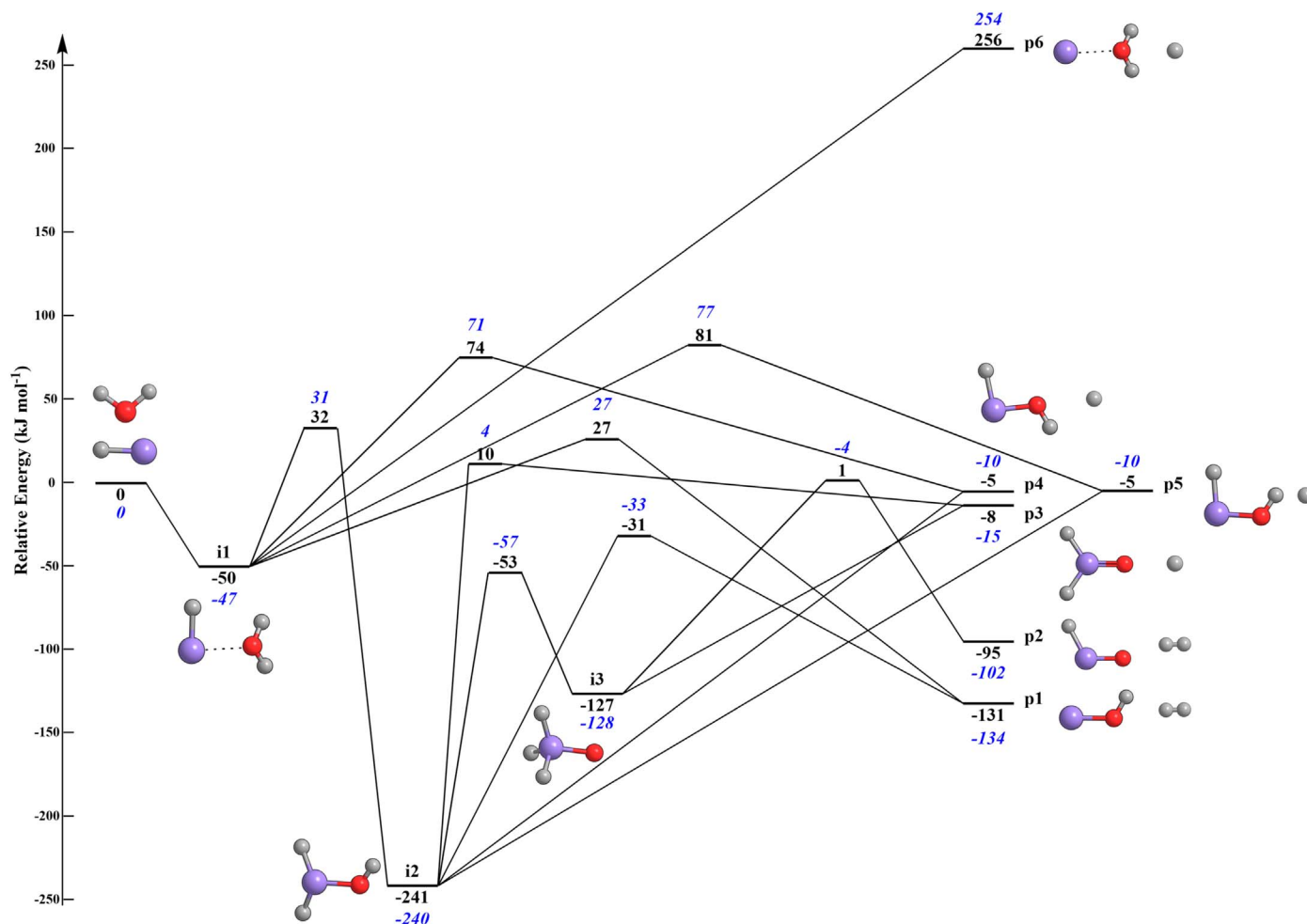


Figure 4. Potential energy diagram of the reaction of the D1-silyldyne radical (SiD; $X^2\Pi$) with D2-water (D_2O) leading to **p1**–**p6**, calculated at the CCSD(T)-F12/cc-pVTZ-f12//B3LYP/6-311G(d,p) + ZPE(B3LYP/6-311G(d,p)) level of theory. The numbers in blue refer to the reaction of the silyldyne radical (SiH; $X^2\Pi$) with water (H_2O). The energies are shown in kJ mol^{-1} with respect to the energy of the separated reactants. Atoms are colored as follows: silicon (purple), oxygen (red), and deuterium (gray). Cartesian coordinates and normal modes are compiled in Table A7.

barrier to the reaction as derived from the line-of-center model (Kaiser et al. 1996; Alagia et al. 2000):

$$\sigma \propto 1 - \frac{E_0}{E_C}. \quad (8)$$

Laboratory investigations of these products are rare. Bogey et al. determined the structure of H_2SiO by rotational submillimeter-wave spectra (Bogey et al. 1996). The experimental results suggest that the bond lengths and angles were $Si=O$ 1.515 Å, $Si-H$ 1.472 Å, and $\angle H-Si-H$ 112° . The $Si=O$ stretching frequency was identified as 1202 cm^{-1} via infrared spectroscopy of H_2SiO in an argon (Ar) matrix (Withnall & Andrews 1985). A frequency of 697 cm^{-1} is also obtained, which is assigned to the SiH_2 wag or SiH_2 rock. Our calculations reveal that, for the H_2SiO molecule, the bond lengths of $Si=O$ and $Si-H$ are 1.528 and 1.483 Å (Figure 1), respectively, along with the $\angle H-Si-H$ of 111.4° , and the $Si=O$ stretching frequency in H_2SiO is 1217 cm^{-1} (Table A7). These experimental identified structure parameters of the H_2SiO molecule are well reproduced in our calculation. Margrave and coworkers performed the reaction of silicon atoms with water in a solid argon matrix at a low temperature of 15 K (Ismail et al. 1982). The final products are confirmed as trans- and cis-HSiOH via the infrared spectrum. The trans-HSiOH carries $Si-O$, $Si-H$, and $O-H$ bond lengths of

1.591 ± 0.100 , 1.521 ± 0.030 , and 0.958 ± 0.005 Å and $\angle H-Si-O$ and $\angle Si-O-H$ of 96.6 ± 4.0 and $114.5 \pm 6^\circ$, respectively. The frequencies of the $H-O$ bond stretch, $H-Si$ bond stretch, HSiO bending, $Si-O$ bond stretch, SiOH bending mode, and out-of-plane torsion mode of trans-HSiOH are 3650.0, 1872.3, 937.0, 850.6, 722.6, and 659.1 cm^{-1} , respectively. Furthermore, the observed frequencies (cm^{-1}) of HSiOD, DSiOD, HSi ^{18}O H, HSi ^{18}O D, and DSi ^{18}O D are also included in this study. Our best computed geometry for HSiOH (Figure 1, Table A7) agrees within these experimental errors.

3. Astrophysical Implications

Our combined crossed molecular beam and high-level electronic structure calculational study provided compelling evidence on the facile formation of d2-silaformaldehyde (D_2SiO) and cis/trans-d2-hydroxysilylene (c/t-DSiOD) under single-collision conditions via the bimolecular gas-phase reaction of the D1-silyldyne radical (SiD; $X^2\Pi$) with D_2O . Since the critical isomerization barrier of $32 \pm 5 \text{ kJ mol}^{-1}$ is involved in this reaction, the mechanism may be open in high-temperature oxygen-rich AGB stars. To evaluate the influence of this reaction on the circumstellar chemistry, astrochemical modeling of the chemistry of oxygen-rich AGB stars was conducted. Rate coefficients for the reaction of silyldyne radicals (SiH) with water (H_2O) were computed over a range of

300–3000 K (Appendix A.2) and fitted with the sum of two de Kooij–Arrhenius expressions (Table A2). Considering the aforementioned energy barriers in the SiH–H₂O system, product formation is only open in the hot, inner CSE, where loss reactions with atomic oxygen (O(³P)) and hydroxyl radicals (OH), as well as photodissociation, are important. The rates of these neutral–neutral reactions were taken from Tokuhashi et al. (1990), the photodissociation rates for H₂SiO were extracted from the OSU09 database (Harada et al. 2010), and the photorates for oxo-silyl (HSiO) and silicon hydroxide (SiOH) were adopted from those of formyl (HCO) and hydroxy-methylidyne (COH) but increased by a factor of 5 to reflect the fact that silicon forms weaker bonds than carbon (Table A4). We note that in cases such as this, where the photodissociation cross sections are unknown, the photodissociation rates are highly uncertain, likely to within an order of magnitude. We report below the results of adopting the same photodissociation rate as for the formyl radical.

The models for the outflow exploited mass-loss rates (MLRs) of 10^{-6} and $8 \times 10^{-6} M_{\odot} \text{ yr}^{-1}$ with an outflow velocity of 15 km s^{-1} . We adopted a radial temperature distribution from Crosas & Menten (1997): $T(r) = 128 \times (10^{15}/r)^{4.7} + 447 \times (10^{15}/r)^{1.05} \text{ K}$, with the radius r given in centimeters. Since few dust grains survive at very high temperatures, a maximum temperature of 1500 K in the outflow was incorporated into the model. The effects of two different density profiles for the gas in the expanding CSE were investigated. One is the usual r^{-2} density distribution appropriate for a spherically expanding wind at constant velocity. The second explores that the flow is clumpy. In particular, we adopt a clump volume filling factor of 0.1 together with a void interclump medium, i.e., a one-component model as fully described in Van de Sande et al. (2018). Our initial fractional abundances of parent molecules at $r = 10^{14} \text{ cm}$ are given in Table A5. These are taken from Agúndez et al. (2020), with the initial SiH₄ abundance from McElroy et al. (2013). We note that silane has only been detected in the CSE of the carbon-rich AGB star IRC+10216. The results for the radial distributions of the fractional abundances of HSiO, SiOH, and H₂SiO are presented in Figure 5 for MLRs of 10^{-6} and $8 \times 10^{-6} M_{\odot} \text{ yr}^{-1}$, respectively, and radial column densities for each of our four models—smooth and one-component outflows—are given in Table A6.

We note here that Gobrecht et al. (2016) studied dust formation driven by periodic shock waves in the inner envelope of the O-rich AGB star IK Tau, which has properties somewhat similar to those in our higher-MLR model. Their calculations cover chemistry between one and 10 stellar radii and indicate that HSiO and H₂SiO can be formed efficiently through successive H-abstraction reactions of SiO with H₂. At four stellar radii, equivalent to our starting radius of 10^{14} cm , their calculated values are roughly 3×10^{-7} and 10^{-6} for HSiO and H₂SiO, respectively. We have run models with these species as parents. In this case, their total column densities can be approximated to within 10% by the product of their initial number density, $n(r_{\text{in}})$, and the initial radius, r_{in} . For an MLR = $10^{-6} M_{\odot} \text{ yr}^{-1}$, for example, the column densities are 2.2×10^{15} and $7.4 \times 10^{15} \text{ cm}^{-2}$ for HSiO and H₂SiO, respectively, much larger than those given by our model. The values of these initiating rate coefficients are not listed in the Gobrecht et al. paper or in the references they cite, but the endothermicity of SiO and H₂ equivalent to a temperature of 40,000 K and would be completely inefficient if introduced to our chemical model.

The radial fractional abundance and the column density of SiOH are about 100 times larger than those of HSiO, reflecting the

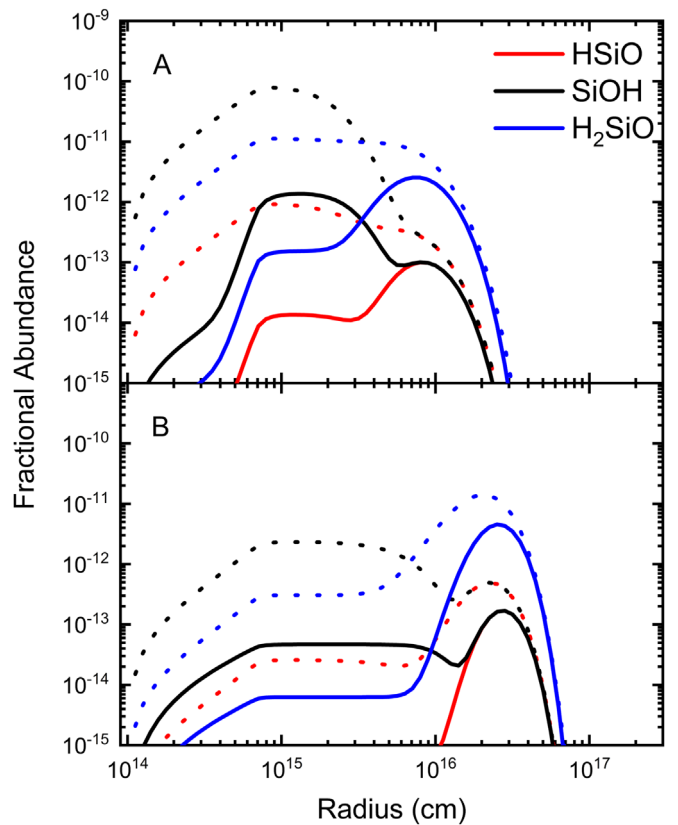


Figure 5. Fractional abundances with respect to molecular hydrogen as a function of radius for MLRs of (a) 10^{-6} and (b) $8 \times 10^{-6} M_{\odot} \text{ yr}^{-1}$. Solid lines: smooth model. Dotted lines: one-component model.

fact that the product channel of the SiH–H₂O system forming HSiO has a smaller preexponential value and larger energy barrier than that of SiOH. Over the range 300–1500 K, the rate coefficient of the channel to SiOH is 5–10 times larger than that to H₂SiO and 50–500 times larger than that to HSiO. The abundances at radii less than about 10^{16} cm are dominated by formation via the SiH–H₂O reaction, while at larger radii, H₂SiO is also formed from the reaction of OH with the silyl radical (SiH₃). The figures show that the one-component models lead to much higher fractional abundances compared to a smooth outflow, with an increase in the column densities of HSiO and SiOH around 100 and H₂SiO around 50 for lower MLRs, to 40 and 10, respectively, for higher MLRs. Although HSiOH has not yet been included in the model calculations due to unknown destruction routes, a rough estimate of its abundance under the assumption that its loss rates are similar to those of H₂SiO can be made so that their relative abundances reflect their relative formation rates, given by their respective formation rate coefficients in Table A2. Over the range 300–1500 K, the rate coefficients to trans-HSiOH and cis-HSiOH are about two and three times greater than that to H₂SiO. Hence, the column density of HSiOH (cis + trans) will be $(0.45\text{--}1.00) \times 10^{11} \text{ cm}^{-2}$ for the one-component models and at least an order of magnitude less for the smooth models. For MLRs greater than $10^{-5} M_{\odot} \text{ yr}^{-1}$, the extinction is so large that the radical species needed to drive the H–Si–O chemistry have low abundances, while for MLRs less than $10^{-6} M_{\odot} \text{ yr}^{-1}$, the extinction is so low that interstellar UV photons destroy species very effectively, and the abundances are also low. We have, in addition, investigated models in which the unshielded photodissociation rates of HSiO, SiOH, and H₂SiO are

factors of 5 smaller. Although this affects the radial fractional abundances, the column densities change by less than a factor of 2. Overall, our detailed calculations show that the reaction between SiH and H₂O can produce HSiO, SiOH, H₂SiO, and cis- and trans-HSiOH in the hot inner CSEs of O-rich AGB stars where the temperature is sufficiently large enough to overcome the substantial energy barriers to these product channels. Fractional abundances and column densities are generally larger in the one-component model due to the larger volume densities and shorter collision times within the clumps.

To sum up, the experiment proceeded at a collision energy of 27.3 kJ mol⁻¹, which represents a temperature of about 3284 K that corresponds to an upper limit for (effective) temperatures prevailing in the circumstellar environment of oxygen-rich stars close to the photosphere. This universal route represents a versatile reaction mechanism to “access” silicon–oxygen molecules through elementary neutral–neutral reactions involving the silylydine radical with oxides. Although not yet quantitatively verified, H₂SiO and HSiOH may photochemically degrade to the astronomically observed SiO (Rizzo et al. 2021). These pathways provide a population of silicon oxides that can possibly be set as a basis for the circumstellar silicates, thus leading us closer to solving the paradox of the injection and destruction timescales of silicates. The formation pathway of SiO in the CSEs of oxygen-rich AGB stars through hydrogenated precursor molecules, which can then be photolyzed to eventually yield SiO, could represent a versatile conceptual pathway to silicon oxides. This route is parallel to the gas-phase preparation of silicon carbides such as silicon trisilicide (c-SiC₃) and silicon tetracarbide (SiC₄) potentially formed via photolysis of their hydrogenated precursors formed in the CSEs of carbon-rich AGB stars (Yang et al. 2019, 2021). Overall, as supported by models, the astronomical detection of H₂SiO and HSiOH in oxygen-rich CSEs and potential correlation with SiO would constrain the high-temperature chemistry and possibly the photochemistry in these oxygen-rich circumstellar environments, thus bringing us closer to the understanding of the most fundamental pathways to (precursors of) grains in circumstellar environments. Finally, we note that future observations of SiOH, HSiO, and/or H₂SiO in the inner regions of O-rich AGB stars would help differentiate between the routes to their formation proposed by us and Gobrecht et al. (2016).

This work at the University of Hawaii was supported by the US National Science Foundation (CHE-1853541). Ab initio and kinetic calculations at Lebedev Physics Institute in Samara were supported by the Ministry of Science and Higher Education of the Russian Federation by grant No. 075-15-2021-597. T.J.M. was supported by the UK Science and Technology Facilities Council through grant ST/P000312/1.

Conflict of interest

The authors declare no conflict of interest.

Appendix

A.1. Experimental Methods

The gas-phase reaction of the D1-silylydine radical (SiD; X²Π) with D₂-water (D₂O; X¹A₁) was studied under single-collision conditions using a universal crossed molecular beam machine at the University of Hawai‘i at Manoa (Kaiser et al. 2010; Yang et al. 2018). In the primary source chamber, a pulsed supersonic D1-silylydine beam was produced in situ by laser ablation of a

Table A1

Peak Velocities (v_p) and Speed Ratios (S) of the D1-silylydine Radical (SiD; X²Π) with D₂-water (D₂O; X¹A₁) Beams along with the Corresponding Collision Energies (E_C) and CM Angles (Θ_{CM}) for the Reactive Scattering Experiment

Beam	v_p (m s ⁻¹)	S	E_C (kJ mol ⁻¹)	Θ_{CM} (deg)
SiD (X ² Π)	1235 ± 30	8.2 ± 2.0		
D ₂ O (X ¹ A ₁)	1738 ± 5	18.8 ± 0.5	27.3 ± 0.5	43.3 ± 0.7

rotating silicon rod at 266 nm, 4 ± 1 mJ pulses (Spectra-Physics Quanta-Ray Pro 270 Nd:YAG laser; 30 Hz), and seeding the ablated species in a gas mixture of deuterium gas (D₂, 99.7%; Icon Isotopes, Inc.) and neon (Ne, 99.999%; Specialty Gases of America) with a ratio of 1:1 and a total pressure of 4 atm. Since the silicon atom has natural isotope abundances (²⁸Si, 92.23%; ²⁹Si, 4.67%; ³⁰Si, 3.10%), the intensity optimization of the D1-silylydine beam was conducted at $m/z = 31$, and no higher molecular weight silicon-/deuterium-bearing species were detected. Although the supersonic beam carries some ground-state silicon atoms (Si(³P)), these silicon atoms (Si(³P)) were found not to react with D₂-water under our experimental conditions. The D1-silylydine beam passed through a skimmer and was velocity-selected by a four-slit chopper wheel, resulting in a well-defined peak velocity (v_p) and speed ratio (S) of 1235 ± 30 m s⁻¹ and 8.2 ± 2.0 (Table A1), respectively. In the secondary source chamber, the pulsed supersonic beam of D₂-water (D₂O, 99.9%; Sigma-Aldrich) seeded in helium (99.9999%; Airgas) at a fraction of 5% at 550 torr with a peak velocity of $v_p = 1738 ± 5$ m s⁻¹ and a speed ratio of $S = 18.8 ± 0.5$ crossed perpendicularly with the primary D1-silylydine beam in the main chamber. This resulted in a collision energy (E_C) of 27.3 ± 0.5 kJ mol⁻¹ and a CM angle (Θ_{CM}) of 43.2 ± 0.7 (Table A1). Each supersonic beam was released by a piezoelectric pulsed valve that was operated at 60 Hz, a pulse width of 80 μs, and a peak voltage of -400 V. Note that even if D1-silylydine radicals in the A²Δ state are formed initially, taking into account the short lifetime of around 500 ns (Bauer et al. 1984), they will decay to the ground-state X²Π during a travel time of about 18 μs to the interaction region in the main chamber.

The neutral reaction products (Figure A1 and Figure A2) entering the detector were ionized by an electron impact ionizer (80 eV; Yang et al. 2018), then filtered according to the mass-to-charge ratio (m/z) utilizing a quadrupole mass spectrometer (Extrel, QC 150) and eventually recorded by a Daly-type ion counter (Yang et al. 2018). The detector is housed within a triply differentially pumped and rotatable chamber that allows the collection of angularly resolved TOF spectra in the plane defined by both reactant beams. To obtain the information on the reaction dynamics, a forward-convolution method was used to transform the laboratory frame data into the CM frame (Yang et al. 2018), which represents an iterative method whereby user-defined CM translational energy $P(E_T)$ and angular $T(\theta)$ flux distributions are varied iteratively until a best fit of the laboratory frame TOF spectra and angular distributions is achieved. These functions comprise the reactive differential cross section $I(\theta, u)$, which is taken to be separable into its CM scattering angle θ and CM velocity u components, $I(u, \theta) \sim P(u) \times T(\theta)$. The error ranges of the $P(E_T)$ and $T(\theta)$ functions are determined within the 1σ limits of the corresponding laboratory angular distribution and beam parameters

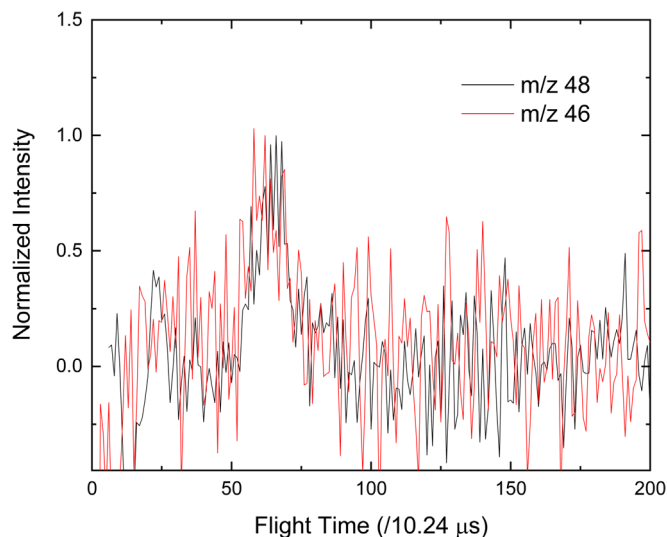


Figure A1. The TOF spectra collected at $m/z = 48$ and 46 for the reaction of the D1-silyldiyne radical (SiD; $X^2\Pi$) with D2-water (D_2O ; X^1A_1) at a CM angle of 44° .

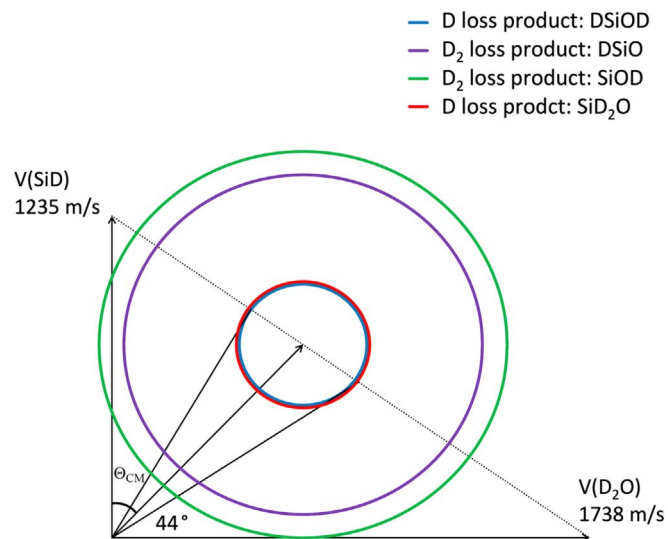


Figure A2. Corresponding Newton diagrams for the reaction of the D1-silyldiyne radical (SiD; $X^2\Pi$) with D2-water (D_2O ; X^1A_1). The circles hold a radius equivalent to the maximum CM velocity of the thermodynamically most stable products, hydroxy-*d*-silyldiyne (SiOD, **p1**, X^1A' , $\Delta_r G = -131 \pm 5$ kJ mol $^{-1}$), oxo-silyl-*d* (DSiO, **p2**, $^1A'$, $\Delta_r G = -95 \pm 5$ kJ mol $^{-1}$), *d2*-silaformaldehyde (D_2SiO , **p3**, X^1A' , $\Delta_r G = -8 \pm 5$ kJ mol $^{-1}$), *cis-d2*-hydroxysilylene (*c*-DSiOD, **p4**, X^1A' , $\Delta_r G = -5 \pm 5$ kJ mol $^{-1}$), and *trans-d2*-hydroxysilylene (*t*-DSiOD, **p5**, X^1A' , $\Delta_r G = -5 \pm 5$ kJ mol $^{-1}$), respectively.

(beam spreads, velocities) while maintaining a good fit to the laboratory TOF spectra.

A.2. Theoretical Methods

Geometries of the reactants, products, intermediates, and transition states involved in the silyldiyne reaction with water were optimized using the hybrid B3LYP (Becke 1993) density functional theory (DFT) method with the 6-311G(d,p) basis set (Table A7). Vibrational frequencies of all species were computed at the same B3LYP/6-311G(d,p) level of theory, taking into account the particular isotopic composition of the $^{28}\text{Si}^{16}\text{O}_3/^{28}\text{Si}^{16}\text{O}_3$ species involved in the SiD + D_2O /SiH

+ H_2O reactions, respectively. For the reactants and critical transition states involved in the pathways for molecular hydrogen loss from the dative complex **i1** (**i1** \rightarrow **p1**) and H atom migration in this complex (**i1** \rightarrow **i2**), geometry optimization was also carried out at the doubly hybrid DFT B2PLYPD3/6-311G(d,p) level of theory (Goerigk & Grimme 2011) incorporating a dispersion correction (Grimme et al. 2011) and at the coupled clusters CCSD/6-311G(d,p) level (Scuseria & Schaefer 1989). For the B2PLYPD3/6-311G(d,p) optimized structures, the vibrational frequencies were recalculated using the same method. Single-point energies were subsequently improved at the explicitly correlated coupled cluster CCSD(T)-F12 level (Knizia et al. 2009) with single and double excitations and perturbative treatment of triple excitations. The CCSD(T)-F12 calculations were carried out with the cc-pVQZ-f12 basis set (Dunning 1989) for most structures, whereas for the critical transition states **i1** \rightarrow **p1** and **i1** \rightarrow **i2**, additional CCSD(T)-F12/cc-pVTZ-f12 calculations were also performed, and the energies were then extrapolated to the complete basis set (CBS) limit using the two-point formula, $E_{\text{CBS}} = E_{\text{cc-pVQZ-f12}} + (E_{\text{cc-pVQZ-f12}} - E_{\text{cc-pVTZ-f12}}) \times 0.69377$ (Martin & Uzan 1998). For the reactants and the two critical transition states, the CCSD(T)-F12/CBS energies were calculated not only for B3LYP but also for B2PLYPD3 and CCSD optimized geometries. For these species, the energies were further refined by taking into account the core electron correlation effects via CCSD(full,T)-F12 calculations with the cc-pCVTZ-f12 and cc-pCVQZ-f12 basis sets (Hill et al. 2010) extrapolated to the CBS limit, which included all core electrons except 1s of Si atoms in the correlation treatment. Finally, anharmonicity corrections to zero-point vibrational energies were evaluated through calculations of anharmonic frequencies at the B3LYP/6-311G(d,p) level of theory using vibrational perturbation theory to the second order (VPT2) (Barone 2005). The B3LYP and B2PLYPD3 calculations, CCSD geometry optimizations, and VPT2 computations of anharmonic frequencies were performed using the GAUSSIAN 09 package (Frisch et al. 2009), whereas the CCSD(T)-F12 calculations were carried out employing MOLPRO 2010 (Werner et al. 2010). It should be noted that the relative CCSD(T)-F12/CBS energies of the **i1** \rightarrow **p1** and **i1** \rightarrow **i2** transition states including the core correlation and anharmonic ZPE corrections with their geometries optimized using B3LYP, B2PLYPD3, and CCSD agreed with the CCSD(T)-F12/cc-pVQZ-f12//B3LYP/6-311G(d,p) + harmonic ZPE(B3LYP/6-311G(d,p)) energies within 1 kJ mol $^{-1}$.

Product branching ratios in the SiD + D_2O reaction under single-collision conditions and at the experimental collision energy of 27.3 kJ mol $^{-1}$ were evaluated using RRKM calculations (Steinfeld et al. 1982) of unimolecular rate constants for the reaction steps beginning with the **i2** intermediate. Here the rate constants were evaluated as functions of the available internal energy of each intermediate or transition state within the harmonic approximation using B3LYP/6-311G(d,p) frequencies, with the internal energy assumed to be equal to the chemical activation energy, that is, negative of the relative energy of a species with respect to the reactants, plus the collision energy. Only one energy level was considered throughout at a zero-pressure limit reproducing the conditions in crossed molecular beams. For the H elimination reaction steps occurring via loose transition states without distinct exit barriers (**i2** \rightarrow **p4/p5** and **i3** \rightarrow **p3**), variational RRKM theory

Table A3
Statistical Branching Ratios (%) for the Reaction of the D1-silyldyne Radical (SiD; X²II) with D2-water (D₂O)^a

p1	p2	p3 (from i2)	p3 (from i3)	p4	p5
41.6	1.0	1.0 (2.0) ^b	12.9 (22.5) ^b	15.2 (26.4) ^b	28.2 (49.1) ^b

Notes.

^a Computed at the experimental collision energy of 27.3 kJ mol⁻¹ considering **i2** as the decomposing intermediate.

^b The numbers in parentheses show branching ratios among the D loss products only.

Table A2
Rate Coefficients of the Silyldyne–Water Reaction as a Sum of Two Modified Arrhenius Expressions: $k = A_1 \times (T/300)^{n_1} \times \exp(-E_1/T) + A_2 \times (T/300)^{n_2} \times \exp(-E_2/T)$

Channel	A_1 (cm ³ s ⁻¹)	n_1	E_1 (K)	A_2 (cm ³ s ⁻¹)	n_2	E_2 (K)
SiOH + H ₂	3.64E-14	2.4619	1748.9	7.56E-16	2.7492	48.044
HSiO + H ₂	1.49E-15	2.1333	2949.0	3.27E-17	2.5685	987.76
H ₂ SiO + H	1.70E-15	3.2836	2175.4	5.33E-17	3.5726	454.71
t-HSiOH + H	5.04E-16	4.1114	1045.4	4.11E-20	4.8323	-1530.4
c-HSiOH + H	1.49E-15	3.7393	1252.6	1.59E-19	4.4594	-1332.5
Total	9.84E-15	3.4025	1040.6	5.27E-17	3.6986	-687.16

(Steinfeld et al. 1982) was employed. Here the minimal energy reaction paths (MEPs) were scanned at the B3LYP/6-311G(d, p) level along the bond distances for the breaking Si–H bonds with all other geometric parameters being optimized. Vibrational frequencies for the optimized structures were then computed at the same level of theory, with the normal mode corresponding to the reaction coordinate projected out. Single-point energies of these MEP structures were recomputed at CCSD(T)-F12/cc-pVQZ-f12. These structures were then considered as transition-state candidates, and rate constants for the H losses from **i2** and **i3** were evaluated with these candidates. In each case, the minimal rate constant was selected as the true rate constant corresponding to a particular collision energy. The conventional and variational RRKM rate constants were used to evaluate product branching ratios by solving first-order kinetic equations within steady-state approximation (Kislov et al. 2004). It should be noted that from the dative complex **i1**, the reaction flux can branch not only to **i2** but also to **p1**, thus increasing the yield of this product. However, since the predicted energies of the **i1** → **p1** and **i1** → **i2** transition states are within our expected error bars of ±5 kJ mol⁻¹ from the experimental collision energy and the D₂ loss product could

not be experimentally detected, we did not consider the **i1** → **p1** pathway in the present calculations, keeping in mind that the computed yield of **p1** (Table A3) is likely underestimated.

Additionally, RRKM master equation (ME) calculations (Fernández-Ramos et al. 2006) were carried out to evaluate temperature-dependent total and individual product channel rate constants for the SiH + H₂O reaction in the temperature range from 300 to 3000 K in the limit of zero pressure (Table A2 and Table A4). The MESS program package (Georgievskii et al. 2013; Georgievskii & Klippenstein 2015) was used for the calculations where the rigid rotor-harmonic oscillator approximation was employed in the evaluation of partition functions. All channels on the PES depicted in Figure 4 were included in the RRKM ME calculations, excluding only the highly unfavorable p6 + H route. Rate constants for the barrierless H elimination channels were assessed using variational RRKM theory as described above. For the astrochemical modeling, the initial fractional abundances of parent molecules and radial column densities for our models are reflected in Tables A5 and A6, respectively.

Table A4
New Reactions and Rate Coefficients Included in Our Chemical Model

Reaction	A ($\text{cm}^3 \text{s}^{-1}$)	n	E (K)	Note
$\text{SiH} + \text{H}_2\text{O} \rightarrow \text{SiOH} + \text{H}_2$				Table A2
$\text{SiH} + \text{H}_2\text{O} \rightarrow \text{HSiO} + \text{H}_2$				Table A2
$\text{SiH} + \text{H}_2\text{O} \rightarrow \text{H}_2\text{SiO} + \text{H}$				Table A2
$\text{O} + \text{SiH}_3 \rightarrow \text{H}_2\text{SiO} + \text{H}$	2.16E-10	0.0	1005.0	Kushner (1993)
$\text{OH} + \text{SiH}_3 \rightarrow \text{H}_2\text{SiO} + \text{H}_2$	8.30E-12	0.0	0.0	Tokuhashi et al. (1990)
$\text{SiOH} + h\nu \rightarrow \text{SiO} + \text{H}$	5.00E-09	0.0	1.7	See text
$\text{HSiO} + h\nu \rightarrow \text{SiO} + \text{H}$	5.00E-09	0.0	1.7	See text
$\text{H}_2\text{SiO} + h\nu \rightarrow \text{SiO} + \text{H}_2$	4.40E-10	0.0	1.6	Harada et al. (2010)
$\text{H}_2\text{SiO} + h\nu \rightarrow \text{HSiO} + \text{H}$	2.20E-10	0.0	1.6	Harada et al. (2010)
$\text{H}_2\text{SiO} + h\nu \rightarrow \text{SiOH} + \text{H}$	2.20E-10	0.0	1.6	Harada et al. (2010)
$\text{O} + \text{HSiO} \rightarrow \text{SiO} + \text{OH}$	1.66E-10	0.0	0.0	Tokuhashi et al. (1990)
$\text{O} + \text{SiOH} \rightarrow \text{SiO} + \text{OH}$	1.66E-10	0.0	0.0	Tokuhashi et al. (1990)
$\text{OH} + \text{HSiO} \rightarrow \text{SiO} + \text{H}_2\text{O}$	1.66E-10	0.0	0.0	Tokuhashi et al. (1990)
$\text{OH} + \text{SiOH} \rightarrow \text{SiO} + \text{H}_2\text{O}$	1.66E-10	0.0	0.0	Tokuhashi et al. (1990)
$\text{OH} + \text{H}_2\text{SiO} \rightarrow \text{HSiO} + \text{H}_2\text{O}$	6.25E-12	0.0	85.4	Kushner (1993)
$\text{OH} + \text{H}_2\text{SiO} \rightarrow \text{SiOH} + \text{H}_2\text{O}$	6.25E-12	0.0	85.4	Kushner (1993)

Note. Rate coefficients are fitted to the modified Arrhenius formula: $k = A \times (T/300)^n \times \exp(-E/T)$.

Table A5
Initial Fractional Abundances of Parent Molecules Relative to H_2

H_2O	2.2E-4	CO	3.0E-4	CO_2	3.0E-7
SO	3.1E-6	SO_2	3.7E-6	SiO	2.7E-5
N_2	4.0E-5	NH_3	6.3E-7	HCN	2.6E-7
H_2S	1.8E-5	CS	5.6E-8	SiS	9.5E-7
SiH_4	2.2E-7	PO	7.8E-8	PN	1.5E-8

Table A6
Radial Column Densities (cm^{-2}) of HSiO, SiOH, and H_2SiO with MLRs in Units of $M_\odot \text{yr}^{-1}$

	$10^{-6} (M_\odot \text{yr}^{-1})$		$8 \times 10^{-6} (M_\odot \text{yr}^{-1})$	
	Smooth	One-component	Smooth	One-component
HSiO	2.18E7	1.56E9	3.48E7	4.85E8
SiOH	1.17E9	1.25E11	8.05E8	3.17E10
H_2SiO	4.44E8	2.04E10	9.41E8	9.14E9

Table A7Optimized Cartesian Coordinates and Vibrational Frequencies for All Intermediates, Transition States, Reactants, and Products Involved in the Reactions of the D1-silylydine Radical (SiD) with D2-water (D₂O)

Species	Vibrational Frequencies (cm ⁻¹)			Cartesian Coordinates (Å)			
				Atom	X	Y	Z
SiH	2014.8481			Si	0.000000	0.000000	0.102349
				H	0.000000	0.000000	-1.432882
SiD	1449.7967						
H ₂ O	1639.2716	3811.1362	3907.5232	O	0.000000	0.000000	0.118805
				H	0.000000	0.756594	-0.475218
				H	0.000000	-0.756594	-0.475218
D ₂ O	1199.4323	2748.1429	2862.1539				
i1 (SiH ₃ O)	163.8095	286.1448	415.8619	O	-1.257160	-0.002868	-0.094400
	488.6573	791.9714	1618.5760	H	-1.617859	0.768975	0.357496
	1982.1953	3791.9061	3895.5162	H	-1.680034	-0.782395	0.283405
				Si	0.896473	-0.099819	0.010210
				H	0.804551	1.433823	-0.028643
i1 (SiD ₃ O)	117.4637	280.3143	310.9353				
	349.0965	586.3287	1186.9695				
	1427.0895	2731.7348	2858.0185				
i2 (SiH ₃ O)	273.0302	678.3959	773.7069	O	-1.081250	-0.108894	0.073658
	822.0908	878.2942	929.0702	H	-1.626269	0.643843	-0.167344
	2127.4851	2203.9087	3889.3263	H	1.130577	-1.241582	0.450287
				Si	0.572474	0.019512	-0.107724
				H	1.131063	1.195733	0.635931
i2 (SiD ₃ O)	199.4387	489.9011	587.5613				
	640.3224	663.3957	848.7412				
	1524.8702	1591.4035	2832.3135				
i3 (SiH ₃ O)	534.9421	554.7793	820.6408	O	-1.193648	0.000497	0.026494
	885.0189	909.4044	1006.3178	Si	0.477062	0.000110	0.002385
	2171.1159	2227.0489	2228.5105	H	1.070649	1.226247	0.591737
				H	0.730099	-0.025321	-1.469464
				H	1.069577	-1.206445	0.632382
i3 (SiD ₃ O)	405.9428	425.2389	637.9514				
	659.7685	712.2999	828.4441				
	1553.9518	1597.4603	1610.1898				
H ₂ SiO	705.8736	711.6375	1023.2253	O	-1.088273	0.000000	0.000000
	1217.3128	2222.6821	2238.5022	Si	0.439901	0.000000	0.000000
				H	1.273785	-1.226725	0.000000
				H	1.273785	1.226725	0.000000
D ₂ SiO	545.2099	548.3482	736.2809				
	1202.6165	1598.3974	1620.9361				
trans-HSiOH	695.4915	799.8918	842.8505	O	-0.027062	1.035054	0.000000
	948.8154	2007.9220	3850.7009	Si	-0.027062	-0.638894	0.000000
				H	-0.904018	1.431685	0.000000
				H	1.499388	-0.767596	0.000000
trans-DSiOD	508.0389	577.8436	709.9203				
	839.4854	1445.9984	2803.7344				
cis-HSiOH	657.1015	713.0332	848.8560	O	-1.030575	-0.094783	0.000000
	964.5395	1912.7466	3846.9066	Si	0.635981	-0.100844	0.000000
				H	-1.517322	0.734954	0.000000
				H	0.858184	1.435123	0.000000
cis-DSiOD	487.9168	508.8808	728.9761				
	848.0702	1376.8725	2801.7423				
HSiO	615.4602	1157.7019	1902.8167	O	0.058836	1.034771	0.000000
				Si	0.058836	-0.503833	0.000000
				H	-1.294392	-1.224509	0.000000
DSiO	463.7706	1153.0591	1371.8020				
SiOH	743.0187	861.6904	3816.9934	O	0.036206	0.992557	0.000000
				Si	0.036206	-0.672658	0.000000
				H	-0.796525	1.476758	0.000000
SiOD	554.3175	847.4712	2780.1795				
Si...H ₂ O (triplet)	263.5334	412.7371	498.2755	O	-1.257659	0.000000	-0.100103
	1617.2647	3781.9714	3882.9591	H	-1.625161	0.774143	0.343288
				H	-1.625156	-0.774146	0.343286
				Si	0.950828	0.000000	0.008161
Si...D ₂ O (triplet)	259.1675	308.6691	361.8375				

Table A7
(Continued)

Species	Vibrational Frequencies (cm^{-1})			Cartesian Coordinates (\AA)			
				Atom	X	Y	Z
Transition state i1 (SiH_3O) \rightarrow SiOH	1184.9672	2724.9481	2848.0461				
	-1400.9151	528.8608	575.5362	O	1.133076	-0.080506	-0.112710
	746.4277	1032.4168	1269.4738	Si	-0.779828	-0.112682	0.005266
	1816.1411	1850.7445	3821.6471	H	1.586424	-0.403996	0.674053
Transition state i1 (SiD_3O) \rightarrow SiOD				H	0.565185	1.070261	0.064584
				H	-0.298617	1.555337	0.089312
	-1019.1304	388.1533	545.1091				
	566.3211	767.8341	908.9180				
Transition state i1 \rightarrow i2 (SiH_3O)	1288.1269	1325.0818	2782.5891				
	-1407.5419	498.4742	585.8171	O	-1.173301	-0.071804	-0.093167
	636.5558	855.7707	988.9698	H	-1.561332	0.797113	0.088421
	1610.1571	2007.0335	3760.4889	H	-0.525862	-0.454681	0.978144
Transition state i1 \rightarrow i2 (SiD_3O)				Si	0.757613	-0.085081	-0.036841
				H	0.867025	1.423132	0.194544
	-1030.6139	416.1471	450.8609				
	499.2646	638.6138	726.5557				
Transition state i1 (SiH_3O) \rightarrow trans-HSiOH	1159.4091	1444.7199	2737.7769				
	-1589.2972	396.8614	530.8728	O	-1.004451	-0.002123	-0.107638
	663.8441	731.6612	855.9851	H	-1.960409	0.795349	0.555062
	1090.4947	2036.9694	3768.3883	H	-1.432679	-0.865697	-0.019752
Transition state i1 (SiD_3O) \rightarrow trans-DSiOD				Si	0.750545	-0.092763	0.044049
				H	0.921058	1.386016	-0.290899
	-1203.2188	291.6748	401.3395				
	496.3244	622.1531	677.0021				
Transition state i1 (SiH_3O) \rightarrow cis-HSiOH	807.6755	1466.3451	2745.1006				
	-1596.5978	346.2718	549.8153	O	-1.011737	-0.002947	-0.114734
	614.9327	709.7792	887.5530	H	-1.373075	0.894739	-0.123617
	1068.7653	1956.7803	3766.9971	H	-1.986170	-0.588000	0.712605
Transition state i1 (SiD_3O) \rightarrow cis-DSiOD				Si	0.751343	-0.117642	-0.003778
				H	0.934335	1.363826	0.381785
	-1211.4184	251.6288	419.3693				
	452.6710	610.4910	703.7977				
Transition state i2 \rightarrow i3 (SiH_3O)	789.0757	1408.9818	2743.6099				
	-1676.1578	579.1946	662.6489	O	1.126169	0.000000	0.134529
	757.7412	899.3652	990.5754	Si	-0.504482	0.000000	-0.036492
	1928.5513	2205.6780	2226.2997	H	0.611146	-0.000004	-1.160180
Transition state i2 \rightarrow i3 (SiD_3O)				H	-1.278872	1.222391	0.297411
				H	-1.278876	-1.222385	0.297417
	-1222.6468	415.0494	505.5388				
	576.9668	706.4093	896.1591				
Transition state i2 (SiH_3O) \rightarrow SiOH	1383.1707	1582.5430	1611.6356				
	-1749.8514	498.6626	572.0371	O	1.070304	0.183968	0.005607
	771.1815	793.9667	895.2493	Si	-0.570273	-0.222402	0.023932
	1436.4522	1633.5555	3857.3788	H	1.641943	-0.569268	-0.171850
Transition state i2 (SiD_3O) \rightarrow SiOD				H	-1.248187	0.964666	-0.808212
				H	-0.972368	1.246487	0.600157
	-1275.1456	366.2297	418.7408				
	558.5353	662.1445	791.8439				
Transition state i2 (SiH_3O) \rightarrow H_2SiO	1023.4244	1176.2372	2808.6873				
	-700.9140	180.4691	292.9968	O	-1.048643	0.170499	0.431625
	690.8302	695.0297	1009.7754	H	-2.122148	0.931260	-0.781565
	1147.6580	2227.0951	2250.6746	H	1.163489	-1.166649	-0.220666
Transition state i2 (SiD_3O) \rightarrow D_2SiO				Si	0.482059	-0.011737	0.410401
				H	1.438324	1.011870	0.894339
	-512.7540	132.2586	223.5982				
	524.6181	539.8339	727.9412				
Transition state i3 (SiH_3O) \rightarrow HSiO	1124.5128	1598.4097	1630.0224				
	-1162.6658	483.8049	628.4198	O	-1.147018	0.091275	0.053280
	819.6700	957.6363	1136.3586	Si	0.374316	-0.121489	-0.081223
	1258.8931	1933.4974	2275.2445	H	1.224900	-1.213129	0.423347
Transition state i3 (SiD_3O) \rightarrow DSiO				H	1.349476	1.070498	-0.383550
				H	1.361341	1.113285	0.671087
	-852.4192	377.4341	487.0344				

Table A7
(Continued)

Species	Vibrational Frequencies (cm ⁻¹)			Cartesian Coordinates (Å)			
				Atom	X	Y	Z
Transition state trans-HSiOH + H → HSiO + H ₂	585.8289	683.4504	904.2556				
	1121.4387	1391.6601	1642.1905				
	-1755.1382	381.9624	418.4205	O	0.847468	0.398251	0.000000
	765.4431	860.9609	978.8453	Si	-0.684173	-0.211160	0.000000
	1093.6062	1474.2482	1967.4913	H	-1.284218	1.201129	0.000000
Transition state trans-DSiOD + D → DSiO + D ₂				H	1.701085	-0.334943	0.000000
	-1271.5678	293.4724	305.3049	H	2.381807	-1.095952	0.000000
	564.5316	701.3010	785.2250				
	845.0513	1085.0419	1415.6973				

ORCID iDs

Shane J. Goettl  <https://orcid.org/0000-0003-1796-5725>
 Ralf I. Kaiser  <https://orcid.org/0000-0002-7233-7206>
 Alexander M. Mebel  <https://orcid.org/0000-0002-7233-3133>
 Tom J. Millar  <https://orcid.org/0000-0001-5178-3656>

References

- Abplanalp, M. J., Gozem, S., Krylov, A. I., et al. 2016, *PNAS*, 113, 7727
 Agúndez, M., Martínez, J. I., de Andres, P. L., Cernicharo, J., & Martín-Gago, J. A. 2020, *A&A*, 637, A59
 Alagia, M., Balucani, N., Cartechini, L., et al. 2000, *PCCP*, 2, 599
 Avramov, P. V., Adamovic, I., Ho, K.-M., et al. 2005, *JPCA*, 109, 6294
 Barone, V. 2005, *JChPh*, 122, 014108
 Bauer, W., Becker, K. H., Düren, R., Hubrich, C., & Meuser, R. 1984, *CPL*, 108, 560
 Becke, A. D. 1993, *JChPh*, 98, 5648
 Bogey, M., Delcroix, B., Walters, A., & Guillemin, J.-C. 1996, *JMoSp*, 175, 421
 Cigan, P., Matsuura, M., Gomez, H. L., et al. 2019, *ApJ*, 886, 51
 Crosas, M., & Menten, K. M. 1997, *ApJ*, 483, 913
 Draine, B. T. 2009, in ASP Conf. Ser. 414, Cosmic Dust—near and Far, ed. T. Henning et al. (San Francisco, CA: ASP), 453
 Dunning, T. H. 1989, *JChPh*, 90, 1007
 Dwek, E. 2016, *ApJ*, 825, 136
 Escatllar, A. M., & Bromley, S. T. 2020, *A&A*, 634, A77
 Fabian, D., Jäger, C., Henning, T., Dorschner, J., & Mutschke, H. 2000, *A&A*, 364, 282
 Fernández-Ramos, A., Miller, J. A., Klippenstein, S. J., & Truhlar, D. G. 2006, *ChRv*, 106, 4518
 Frisch, M. J., Trucks, G. W., Schlegel, H. B., et al. 2009, Gaussian 09, Revision D.01 (Gaussian Inc.: Wallingford, CT 2009, 200, 28.)
 Fu, B., Han, Y.-C., Bowman, J. M., et al. 2012, *JChPh*, 137, 22A532
 Gail, H.-P., & Sedlmayr, E. 1999, *A&A*, 347, 594
 Gail, H.-P., Wetzel, S., Pucci, A., & Tamanai, A. 2013, *A&A*, 555, A119
 Georgievskii, Y., & Klippenstein, S. J. 2015, *PAPR*: Predictive Automated Phenomenological Rates, <https://tcg.cse.anl.gov/papr>
 Georgievskii, Y., Miller, J. A., Burke, M. P., & Klippenstein, S. J. 2013, *JPCA*, 117, 12146
 Glenewinkel-Meyer, T., Bartz, J. A., Thorson, G. M., & Crim, F. F. 1993, *JChPh*, 99, 5944
 Gobrecht, D., Cherchneff, I., Sarangi, A., Plane, J. M. C., & Bromley, S. T. 2016, *A&A*, 585, A6
 Goerigk, L., & Grimme, S. 2011, *J. Chem. Theory Comput.*, 7, 291
 Goumans, T. P. M., & Bromley, S. T. 2012, *MNRAS*, 420, 3344
 Grimme, S., Ehrlich, S., & Goerigk, L. 2011, *JCoCh*, 32, 1456
 Harada, N., Herbst, E., & Wakelam, V. 2010, *ApJ*, 721, 1570
 Henning, T. 2010, *ARA&A*, 48, 21
 Hill, J. G., Mazumder, S., & Peterson, K. A. 2010, *JChPh*, 132, 054108
 Ismail, Z. K., Hauge, R. H., Fredin, L., Kauffman, J. W., & Margrave, J. L. 1982, *JChPh*, 77, 1617
 Jones, A. P., & Nuth, J. A. 2011, *A&A*, 530, A44
 Kaiser, R. I., Lee, Y. T., & Suits, A. G. 1996, *JChPh*, 105, 8705
 Kaiser, R. I., Maksyutenko, P., Ennis, C., et al. 2010, *FaDi*, 147, 429
 Kislov, V. V., Nguyen, T. L., Mebel, A. M., Lin, S. H., & Smith, S. C. 2004, *JChPh*, 120, 7008
 Knizia, G., Adler, T. B., & Werner, H.-J. 2009, *JChPh*, 130, 054104
 Krasnokutski, S. A., Rouillé, G., Jäger, C., et al. 2014, *ApJ*, 782, 15
 Kushner, M. J. 1993, *JAP*, 74, 6538
 Levine, R. D. 2005, *Molecular Reaction Dynamics* (Cambridge: Cambridge Univ. Press)
 Li, A., & Draine, B. T. 2002, *ApJ*, 564, 803
 Liu, J., & Jiang, B. 2017, *AJ*, 153, 176
 Loeffler, M. J., Dukes, C. A., Christoffersen, R., & Baragiola, R. A. 2016, *M&PS*, 51, 261
 Martin, J. M. L., & Uzan, O. 1998, *CPL*, 282, 16
 Mazarei, E., & Mousavipour, S. H. 2017, *JPCA*, 121, 8033
 McElroy, D., Walsh, C., & Markwick, A. J. 2013, *A&A*, 550, A36
 Miller, W. B., Safron, S. A., & Herschbach, D. R. 1967, *FaDi*, 44, 108
 Nozawa, T., Kozasa, T., Ishii, T. T., & Takeuchi, T. T. 2005, *MNRAS*, 357, 1077
 Reber, A. C., Clayborne, P. A., Reveles, J. U., et al. 2006, *NanoL*, 6, 1190
 Reber, A. C., Paranthaman, S., Clayborne, P. A., Khanna, S. N., & Castleman, A. W., Jr 2008, *ACS nano*, 2, 1729
 Rizzo, J. R., Cernicharo, J., & García-Miró, C. 2021, *ApJS*, 253, 44
 Schneider, R., Ferrara, A., & Salvaterra, R. 2004, *MNRAS*, 351, 1379
 Scuseria, G. E., & Schaefer, H. F., III 1989, *JChPh*, 90, 3700
 Simmie, J. M., & Würmel, J. 2020, *JPCRD*, 49, 023102
 Steinfeld, J. I., Francisco, J. S., & Hase, W. L. 1982, *Chemical Kinetics and Dynamics*, Vol. 3 (New Jersey: Prentice Hall Englewood Cliffs)
 Takigawa, A., Kamizuka, T., Tachibana, S., & Yamamura, I. 2017, *SciA*, 3, eao2149
 Tielens, A. G. G. M. 1998, *ApJ*, 499, 267
 Tielens, A. G. G. M. 2012, in *Nature's Nanostructures*, ed. A. S. Barnard & H. Guo (Singapore: Pan Stanford Publishing Pte. Ltd.)
 Tokuhashi, K., Horiguchi, S., Urano, Y., et al. 1990, *CoFI*, 82, 40
 Van de Sande, M., Sundqvist, J. O., Millar, T. J., et al. 2018, *A&A*, 616, A106
 Wakelam, V., Smith, I. W. M., Herbst, E., et al. 2010, *SSRv*, 156, 13
 Werner, H. J., Knowles, P. J., Lindh, R., et al. 2010, *MOLPRO*, Version 2010.1 (Univ. College Cardiff Consultants Ltd: United Kingdom, 2010)
 Withnall, R., & Andrews, L. 1985, *JPhCh*, 89, 3261
 Yang, T., Bertels, L., Dangi, B. B., et al. 2019, *PNAS*, 116, 14471
 Yang, T., Thomas, A. M., Dangi, B. B., et al. 2018, *NatCo*, 9, 774
 Yang, Z., Doddipatla, S., Kaiser, R. I., et al. 2021, *ApJL*, 908, L40
 Zachariah, M. R., & Tsang, W. 1995, *JPC*, 99, 5308
 Ziurys, L. M. 2006, *PNAS*, 103, 12274